

Criticality of biochemical feedback

Amir Erez,^{1,*} Tommy A. Byrd,^{2,*} Robert M. Vogel,³ Grégoire Altan-Bonnet,¹ and Andrew Mugler^{2,†}

¹*Immunodynamics Group, Cancer and Inflammation Program, National Cancer Institute, National Institutes of Health, Bethesda, Maryland 20814, USA*

²*Department of Physics and Astronomy, Purdue University, West Lafayette, Indiana 47907, USA*

³*IBM T. J. Watson Research Center, Yorktown Heights, New York 10598, USA*

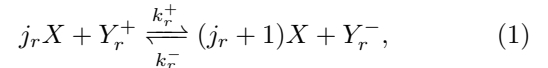
Biochemical feedback leads to dynamical transitions between cellular states, reminiscent of phase transitions in equilibrium systems. Yet cells are far from equilibrium. Here we show using a generic birth-death model that despite being far from equilibrium, biochemical feedback near a bifurcation point exhibits the scaling exponents of the mean-field universality class. The theory allows us to calculate an effective order parameter, temperature, external field, and heat capacity from T cell fluorescence data without fitting. Experiments agree with the scaling predictions, suggesting that this type of nonequilibrium criticality plays an important role in cell biology.

Living cells are nonequilibrium systems. Yet some cellular behaviors are reminiscent of equilibrium physical phenomena. A key example is biochemical feedback: positive feedback at the gene regulatory or signaling level can lead to a transition from one to two functional states, modeled as a bifurcation in a dynamical system or its stochastic analog [1, 2]. This behavior is reminiscent of a phase transition in an equilibrium statistical system such as a fluid, magnet, or superconductor, where a disordered state transitions to one of two ordered states at a critical temperature [3]. The bifurcation point is the analog of the critical point. Yet critical points in equilibrium statistical systems satisfy very specific criteria, such as scaling laws, that place them in particular universality classes [3]. This raises a fundamental question: what, if any, features of criticality, in the strict statistical physics sense, are exhibited by a biochemical system with feedback near its dynamical transition point?

Recent experiments have shown that biological systems on all scales, from molecules [4], to cells [5–8], to populations [9, 10], exhibit signatures consistent with equilibrium criticality. However, the details of how to map these systems to effective equilibrium systems are often unclear, and some of these signatures can be alternatively explained without relying on proximity to criticality [11, 12]. This highlights the need for a theoretical framework that maps a nonequilibrium biological system to an equilibrium system in a rigorous, falsifiable way.

Here we investigate the statistical physics of biochemical feedback near its dynamical transition point. We focus on a generic stochastic framework in which feedback is encapsulated in a birth-death process. We show that, despite being far from equilibrium, the system exhibits near its transition point the critical properties of the mean-field universality class. Our theory gives quantitative predictions that we test, without fitting, using data on T cell signaling measured at the single-cell level [13]. The agreement of theory and experiment suggests that the critical behavior we uncover here plays an important role in immune response, and in cellular networks in general.

Consider a reaction network in a cell, where X is the molecular species of interest, and A, B, C , etc. are the other species [Fig. 1(a)]. The other species form a chemical “bath” for X . The reactions of interest produce or degrade an X molecule, can involve the bath species, and in principle are reversible. We allow for nonlinear feedback on X , meaning that the production of an X molecule in a particular reaction might require a certain number of X molecules as reactants. This leads to a general set of R reactions of the form



where in each reaction $r \in \{1, 2, \dots, R\}$, the $j_r \in \{0, 1, 2, \dots\}$ are stoichiometric integers describing the nonlinearity, k_r^\pm are the forward (+) and backward (–) reaction rates, and Y_r^\pm represent the particular bath species involved as reactants (+) or products (–). A simple and well-studied special case of Eq. 1 is the Schlögl model [14, 15], in which X is either produced spontaneously from bath species A , or in a trimolecular reaction from two existing X molecules and bath species B (i.e., $R = 2$, $j_1 = 0$, $j_2 = 2$, $Y_1^+ = A$, $Y_2^+ = B$, and $Y_1^- = Y_2^- = \emptyset$). Since every reaction in Eq. 1 involves the birth or death of one X molecule, the master equation for the probability of observing n such molecules is

$$\dot{p}_n = b_{n-1}p_{n-1} + d_{n+1}p_{n+1} - (b_n + d_n)p_n, \quad (2)$$

where $b_n = \sum_{r=1}^R J_{rn}^+$ and $d_n = \sum_{r=1}^R J_{rn}^-$ are the total birth and death propensities, and $J_{rn}^+ = k_r^+ n_r^+ n! / (n - j_r)!$ and $J_{rn}^- = k_r^- n_r^- n! / (n - j_r - 1)!$ are the forward and backward propensities of each reaction pair. Here n_r^\pm are the numbers of molecules of the bath species involved in reaction r , and the factorials account for the number of ways that X molecules can meet in a well-mixed reaction. We assume that the reaction rates and the numbers of bath molecules are constants in the model.

The steady state of Eq. 2 is

$$p_n = p_0 \prod_{j=1}^n \frac{b_{j-1}}{d_j} = \frac{p_0}{n!} \prod_{j=1}^n f_j, \quad (3)$$

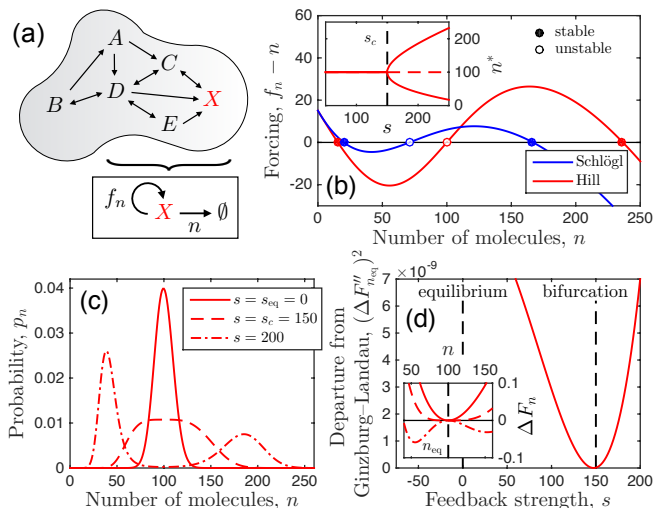


FIG. 1: (a) A generalized feedback function f_n (b) produces either one or two stable steady states, (c) corresponding to distributions that are one- or two-peaked, respectively, or flat at the bifurcation point. (d) Despite being far from equilibrium, the system behaves “canonically” at the bifurcation point, as described in the text. Parameters are $H = 3$, $K = 126$, and $a = n_{\text{eq}} - s/3$ with $n_{\text{eq}} = 100$; in (b) $s = 255$. Legend in (c) also applies to inset of (d).

where $p_0^{-1} = \sum_{n=0}^{\infty} (1/n!) \prod_{j=1}^n f_j$ is set by normalization. In the second step of Eq. 3 we recognize that p_n depends only on the ratio of birth and death propensities, and therefore we define an effective birth propensity $f_n \equiv nb_{n-1}/d_n$ corresponding to spontaneous death with propensity n [Fig. 1(a)]. The function f_n encodes the feedback in our model. For the Schlögl model, the feedback function is

$$f_n = \frac{aK^2 + s(n-1)(n-2)}{(n-1)(n-2) + K^2} \quad (\text{Schlögl}), \quad (4)$$

where we have introduced the dimensionless quantities $a \equiv k_1^+ n_A / k_1^-$, $s \equiv k_2^+ n_B / k_2^-$, and $K^2 \equiv k_1^- / k_2^-$. In general, f_n is an arbitrary, nonlinear function governed by the reaction network. As a generic example we also consider the Hill function with coefficient H ,

$$f_n = a + s \frac{n^H}{n^H + K^H} \quad (\text{Hill}). \quad (5)$$

The quantity $f_n - n$ determines the dynamic stability. It is plotted for Eqs. 4 and 5 in Fig. 1(b). In both cases, we see three steady states n^* where $f_{n^*} - n^* = 0$, two of which are stable (negative slope). Depending on the parameters, there can be either one or two stable states. For example, when a and s are covaried to the Hill function, a transition from a monostable to a bistable regime occurs at the bifurcation point s_c [Fig. 1(b) inset]. Stochastically, these regimes correspond to unimodal and

bimodal distributions p_n , respectively, while the bifurcation point corresponds to a distribution that is flat on top [Fig. 1(c)].

Thermodynamic equilibrium occurs when the system obeys detailed balance, meaning that the forward flux balances the backward flux for every reaction r , i.e. $J_{r,n-1}^+ p_{n-1} = J_{rn}^- p_n$. Inserting the expressions for J_{rn}^\pm (see Eq. 2), this condition becomes $p_n/p_{n-1} = J_{r,n-1}^+/J_{rn}^- = k_r^+ n_r^+ / (k_r^- n_r^- n)$. Since p_n/p_{n-1} is not r -dependent, $k_r^+ n_r^+ / (k_r^- n_r^-)$ is constant for all r , which provides the constraints on the reaction rates that prevent flux cycles from forming in the state space. Calling this constant n_{eq} , we have $p_n/p_{n-1} = n_{\text{eq}}/n$, which is solved by $p_n^{\text{eq}} = e^{-n_{\text{eq}}} (n_{\text{eq}})^n / n!$. We see that the equilibrium distribution is the Poisson distribution [15, 16], corresponding, from Eq. 3, to a constant feedback function $f_n = n_{\text{eq}}$ [see Fig. 1(c) with $s = s_{\text{eq}} = 0$]. This is expected, since in equilibrium the system obeys the grand canonical distribution, which when summed over energies is the Poisson distribution [17].

Out of equilibrium, it is tempting to follow time-dependent Ginzburg–Landau theory [18, 19] and interpret Eq. 3 in the language of the canonical distribution: $p_n \propto e^{-U_n}$, where U_n is a dimensionless “energy,” and $F_n = -\partial_n U_n = \partial_n \log p_n$ is the associated dimensionless “force.” At the same time, Fig. 1(b) independently suggests a force that is proportional to $f_n - n$, namely $\tilde{F}_n = -\partial_n \tilde{U}_n = (f_n - n)/n_{\text{eq}}$. The proportionality factor $1/n_{\text{eq}}$ is set by the fact that when $f_n = n_{\text{eq}}$ at equilibrium, $\tilde{p}_n \propto e^{-\tilde{U}_n}$ should be the Gaussian approximation to the Poisson p_n . Yet, out of equilibrium, we cannot assume that p_n obeys the canonical distribution (even in equilibrium it is *grand* canonical). Therefore, F_n and \tilde{F}_n are, in general, different. Indeed, van Kampen emphasizes that only for diffusion-like processes, where the scale of fluctuations is set by a constant temperature, are U_n and \tilde{U}_n (and thus F_n and \tilde{F}_n) the same; for birth-death processes like the one we study here, where fluctuations scale with molecule number, they are different [20]. However, we see in the inset of Fig. 1(d) that at the bifurcation point s_c (dashed), the difference $\Delta F_n = F_n - \tilde{F}_n$ becomes small, especially around n_{eq} . We quantify this observation by computing the squared curvature $(\Delta F_{n_{\text{eq}}}'')^2$. Indeed, in Fig. 1(d) we see that this measure vanishes at the bifurcation point. Evidently, our system at its nonequilibrium bifurcation point behaves like an equilibrium Ginzburg–Landau system at its critical point.

This behavior can be understood immediately from Eq. 3. For large n we have $F_n = \partial_n \log p_n \approx \log f_n - \log n = \log[1 + (f_n - n)/n]$. At the bifurcation point, f_n is tangent to n at n_{eq} . This creates the largest range of n over which $f_n - n$ is small, which permits the expansion of F_n around n_{eq} as $F_n \approx (f_n - n)/n_{\text{eq}} = \tilde{F}_n$. Thus, at the bifurcation point the two forces agree. This leads to our central question: what, if any, features of criticality does our nonequilibrium biochemical system inherit from its

equilibrium counterpart?

To address this question, we investigate the scaling properties of p_n . The extrema satisfy $0 = \partial_n p_n$, or equivalently $0 = \partial_n \log p_n = F_n \approx \tilde{F}_n \propto f_n - n$, where we have seen that the approximation is valid near the bifurcation point. We expand f_n to third order around a point n_c that we are free to choose. Anticipating a mapping to an equilibrium system, we choose n_c such that $f''_{n_c} = 0$ as in the Ginzburg–Landau critical point. The condition for extrema n_* becomes $0 = f_{n_c} + f'_{n_c}(n_* - n_c) + f'''_{n_c}(n_* - n_c)^3/3! - n_*$. We then define the parameters

$$m \equiv \frac{n_* - n_c}{n_c}, \quad h \equiv \frac{2(f_{n_c} - n_c)}{-f'''_{n_c} n_c^3}, \quad \theta \equiv \frac{2(1 - f'_{n_c})}{-f'''_{n_c} n_c^2}, \quad (6)$$

in terms of which the condition becomes

$$0 = h - \theta m - \frac{1}{3} m^3. \quad (7)$$

Eq. 7 is equivalent to the expansion of the Ising mean field equation $m = \tanh[(m + h)/(1 + \theta)]$ for small magnetization m , where $\theta = (T - T_c)/T_c$ is the reduced temperature, and h is the magnetic field times the magnetic moment over the product of the coupling energy and coordination number [19]. Therefore in our system we interpret m as the order parameter, θ as a reduced “temperature,” and h as a dimensionless “field.” θ refers to an effective temperature, distinct from the actual temperature of the system when it is in equilibrium. Positive (negative) θ drives the system to the unimodal (bimodal) state, while positive (negative) h biases the system to high (low) molecule numbers. Indeed, the covariation of a and s in Fig. 1 is determined by the condition $h = 0$ (see Table S1 [21]). The fact that the high-molecule number peak in Fig. 1(c) is fatter and lower than the low-molecule number peak is due to the scaling of fluctuations with molecule number in a birth-death process.

Eq. 7 implies that our system has the same scaling exponents β , γ , and δ as the mean-field universality class, of which the mean-field Ising model is a member [19]. Specifically, when $h = 0$, Eq. 7 becomes $0 = m(\theta + m^2/3)$; thus the maxima of p_n satisfy $m = 0$ or $m = \pm(-3\theta)^\beta$ when $\theta > 0$ or $\theta < 0$, respectively, with $\beta = 1/2$. Defining the dimensionless susceptibility $\chi \equiv (\partial_h m)_{h=0}$ and differentiating Eq. 7 gives $\chi = \theta^{-\gamma}$ or $\chi = (-2\theta)^{-\gamma}$ for $\theta > 0$ or $\theta < 0$, respectively, with $\gamma = 1$. Finally, when $\theta = 0$, Eq. 7 becomes $m = (3h)^{1/\delta}$, with $\delta = 3$. These scaling results are tested for the Schlögl and Hill models in Fig. 2(a)-(c), and we see excellent agreement.

The exponent α concerns the heat capacity, $C|_{h=0} \sim |\theta|^{-\alpha}$. The equilibrium definition $C = T\partial_T S$ generalizes to nonequilibrium when one uses the Shannon entropy $S = -k_B \sum_n p_n \log p_n$ [22]. In our case $T = (1 + \theta)T_c$ is

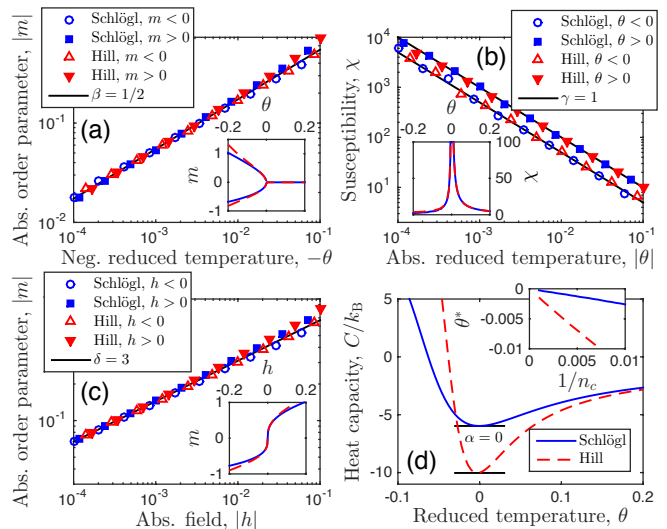


FIG. 2: Critical exponents α , β , γ , and δ of biochemical feedback near its nonequilibrium bifurcation point agree with those of the mean-field universality class. Parameters are $H = 3$; $n_c = 500$; $h = 0$ in (a), (b), and (d); $\theta = 0$ in (c); and K , a , and s calculated from n_c , θ , and h according to Eq. 6 (see Table S1 [21]). (b) uses $m < 0$ maximum for $\theta < 0$; results are similar for $m > 0$. Legend in (d) also applies to all insets.

the effective temperature, such that $C = (1 + \theta)\partial_\theta S$, or

$$\frac{C}{k_B} = -(1 + \theta) \sum_{n=0}^{\infty} p_n (1 + \log p_n) \left(\psi_n - \sum_{j=0}^{\infty} p_j \psi_j \right), \quad (8)$$

where $\psi_n \equiv (1/2)f'''_{n_c} n_c^2 \sum_{j=1}^n (j - n_c)/f_j$. Eq. 8 follows from performing the θ derivative using the expression in Eq. 3, the expansion above Eq. 6, and the definition of θ (Eq. 6). Testing α is more stringent than testing β , γ , and δ , since C is a function not just of the extrema of p_n , but of the entire distribution. We see in Fig. 2(d) that when $h = 0$, C exhibits a minimum at θ^* , and the inset shows that θ^* vanishes as the system size increases, $n_c \rightarrow \infty$. This implies $C|_{h=0} \sim |\theta|^0$ to sub-quadratic order in θ , or $\alpha = 0$, again consistent with the mean-field universality class. Interestingly, whereas C is discontinuous in the mean-field Ising model [19] and constant in the van der Waals model of a fluid [3], it is minimized here; nevertheless, in all cases $\alpha = 0$. C is negative near $\theta = 0$ [Fig. 2(d)]; negative heat capacity is a well-known feature of nonequilibrium steady states [23–25].

We test our theory against experiments using measurements in T cells of doubly phosphorylated ERK (ppERK), which is subject to feedback via the MAP-kinase signaling cascade [13]. Six chemotherapy drugs inhibit key enzymes in the cascade (MEK, SRC), leading to either bimodal (low dose) or unimodal (high dose) distributions of ppERK abundance, measured as fluorescence intensity I by flow cytometry [Fig. 3(a)] [13, 21].

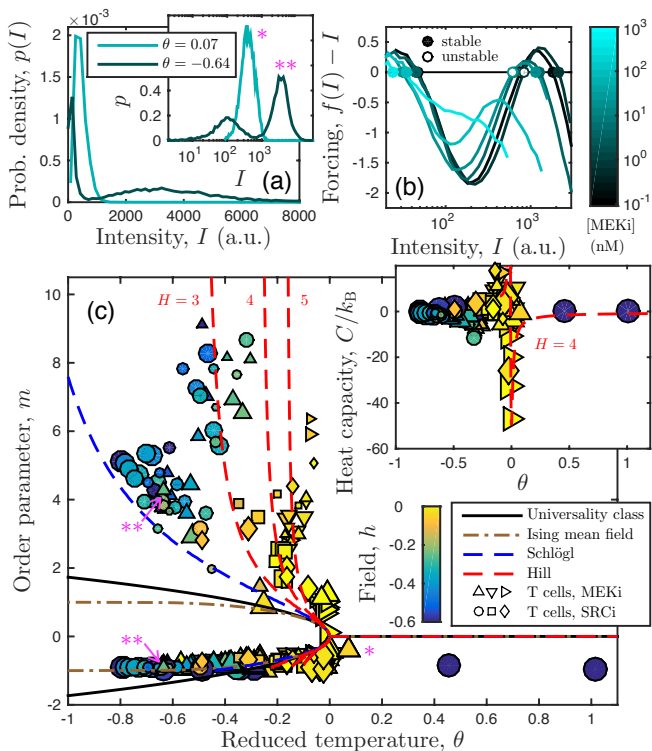


FIG. 3: Comparing theory and experiment. (a) Experimental distributions of T cell ppERK fluorescence intensity are bimodal (unimodal) under low (high) doses of inhibitor. Legend shows θ calculated by Eq. 6. (b) Feedback functions extracted from distributions yield criticality parameters (Eq. 6, 8). (c) Order parameter and heat capacity data agree with theory, particularly for $h \approx 0$ (yellow data) where theory is shown. See Table S2 [21] for drugs (shape) and doses (size). Magenta asterisks indicate data points in (c) corresponding to distributions in (a). Parameters are $W/L = 25/100$ in (b) and (c), $I_1 = 0.1$ in inset of (c), and $h = 0$ and $n_c = 7,300$ (mean experimental value) for Schlögl and Hill models.

We anticipate that applying the drugs is similar to tuning the temperature and/or field in the theory. We derive these parameters from the intensity distributions using the following procedure (see Supplementary Information for full details [21]). First, we set $n = I/I_1$, where the intensity of one molecule I_1 is determined as described shortly. Next, we invert Eq. 3 to obtain the effective feedback function $f_n = np_n/p_{n-1}$ from the distribution [26]. Because the distributions are long-tailed, we calculate f from $\log I$ for numerical stability [Fig. 3(a) inset]. Additionally we smooth f and its derivatives using a Savitzky–Golay filter [27] with window size W . Finally, we calculate m , θ , and h from f (Eq. 6), and C from f and p_n (Eq. 8). This procedure requires the adjustable parameter W/L , where L is the number of $\log I$ bins, but no fitting. Results are robust to W/L [21].

Several expected results validate the analysis. First, distributions with $\theta > 0$ are unimodal (high dose), while

bimodal distributions (low dose) have $\theta < 0$ [Fig. 3(a)]. Second, as expected from Fig. 1(b), we see in Fig. 3(b) that the quantity $f(I) - I$ has one stable state when the distribution is unimodal (light cyan), and two stable states when the distribution is bimodal (dark cyan). Third, as found previously [13], the location of the high stable state changes with MEK inhibitor but not SRC inhibitor [21].

Fig. 3(c) shows the $h = 0$ predictions from the theory (blue and red), the mean-field Ising model (brown), and the universality class to which they belong (Eq. 7; black). All coincide at the critical point ($m = \theta = 0$). The lower branches ($m < 0$) of the biochemical and Ising models obey $m \geq -1$ because the number of molecules and up-spins is nonnegative, respectively (Eq. 6). Whereas the upper branch ($m > 0$) of the Ising model obeys $m \leq 1$ since the total number of spins is fixed, those of the biochemical models rise steeply since the molecule number is unbounded from above. The data points in Fig. 3(c) show m vs. θ for all drugs (shape) and doses (size), colored according to h . Most data have $\theta \lesssim 0$, since doses are sufficiently low to maintain a non-negligible high state; and $h \lesssim 0$, due to the long tails and the possible impact of autofluorescence [21]. We see that the data agree with the predictions in several important ways: (i) no data exist between the branches; (ii) data near $m = \theta = 0$ have $h \approx 0$ (yellow); (iii) the data closely follow the lower branch and obey $m \geq -1$; and (iv) the data exhibit the steep rise of the upper branches in the biochemical models, particularly the Hill function with $H \sim 4$.

The inset of Fig. 3(c) shows the $h = 0$ prediction for C with $H = 4$ (red), along with the data. We see that the two agree, particularly for data with $h \approx 0$ (yellow) as expected. A key feature for criticality, a global minimum in C at $\theta = h = 0$, is exhibited by the data and is robust to the choice of I_1 over four orders of magnitude [21]. Importantly, the depth of the minimum agrees with that of the theory only for $I_1 \sim 0.1$ as in the inset, corresponding to $n_* \approx 35,000$ molecules in the high mode without inhibition [21], in agreement with previous measurements on these cells [28]. Thus the heat capacity allows estimation of absolute molecule number from fluorescence data. The agreement between theory and data in Fig. 3(c) is especially striking given that the theory is derived assuming a birth-death process, whereas the experimental distributions show long tails suggestive of more complex mechanisms such as bursting [29, 30] or cell-to-cell variability [31]. This suggests that the critical behavior we identify is universal, applicable to biochemical feedback beyond even the generic model we consider.

We have shown that a generic model of biochemical feedback exhibits the scaling properties of the mean-field universality class near its dynamic transition point, despite being far from equilibrium. By discovering the effective order parameter, temperature, external field, and heat capacity of the system, we have quantitatively trans-

lated both the model and T cell fluorescence data into the language of statistical physics. Doing so has revealed agreement between the data and falsifiable predictions of the theory, with no fitting, suggesting that this class of nonequilibrium critical behavior plays an important role in cell biology. It will be interesting to see whether our framework allows one to unite diverse biological systems under one or several universality classes.

This work was supported by Human Frontier Science Program grant LT000123/2014 (A. E.) and Simons Foundation grant 376198 (T. B. and A. M.).

* These authors contributed equally.

† Electronic address: amugler@purdue.edu

- [1] J. Hornos, D. Schultz, G. Innocentini, J. Wang, A. Walczak, J. Onuchic, and P. Wolynes, *Physical Review E* **72**, 051907 (2005).
- [2] G. Tkačik, A. M. Walczak, and W. Bialek, *Physical Review E* **85**, 041903 (2012).
- [3] N. Goldenfeld, *Lectures on phase transitions and the renormalization group*, vol. 5 (Addison-Wesley Reading, MA, 1992).
- [4] T. Mora, A. M. Walczak, W. Bialek, and C. G. Callan, *Proceedings of the National Academy of Sciences* **107**, 5405 (2010).
- [5] D. B. Kastner, S. A. Baccus, and T. O. Sharpee, *Proceedings of the National Academy of Sciences* **112**, 2533 (2015).
- [6] D. Krotov, J. O. Dubuis, T. Gregor, and W. Bialek, *Proceedings of the National Academy of Sciences* **111**, 3683 (2014).
- [7] G. De Palo, D. Yi, and R. Endres, *bioRxiv* p. 086538 (2016).
- [8] X. Chen, X. Dong, A. Be'er, H. L. Swinney, and H. Zhang, *Physical Review Letters* **108**, 148101 (2012).
- [9] W. Bialek, A. Cavagna, I. Giardina, T. Mora, O. Pohl, E. Silvestri, M. Viale, and A. M. Walczak, *Proceedings of the National Academy of Sciences* **111**, 7212 (2014).
- [10] A. Attanasi, A. Cavagna, L. Del Castello, I. Giardina, S. Melillo, L. Parisi, O. Pohl, B. Rossaro, E. Shen, E. Silvestri, et al., *Physical Review Letters* **113**, 238102 (2014).
- [11] D. J. Schwab, I. Nemenman, and P. Mehta, *Physical Review Letters* **113**, 068102 (2014).
- [12] D. A. Kessler and H. Levine, *arXiv preprint arXiv:1508.02414* (2015).
- [13] R. M. Vogel, A. Erez, and G. Altan-Bonnet, *Nature Communications* **7**, 12428 (2016).
- [14] F. Schlögl, *Zeitschrift für Physik* **253**, 147 (1972).
- [15] M. Vellela and H. Qian, *Journal of the Royal Society Interface* **6**, 925 (2009).
- [16] C. W. Gardiner et al., *Handbook of stochastic methods*, vol. 3 (Springer Berlin, 1985).
- [17] C. Kittel and H. Kroemer, *Thermal physics* (1998).
- [18] P. C. Hohenberg and B. I. Halperin, *Reviews of Modern Physics* **49**, 435 (1977).
- [19] P. Kopietz, L. Bartosch, and F. Schütz, *Introduction to the functional renormalization group*, vol. 798 (Springer, 2010).
- [20] N. G. Van Kampen, *Stochastic processes in physics and chemistry*, vol. 1 (Elsevier, 1992).
- [21] See Supplementary Information.
- [22] D. Mandal, *Physical Review E* **88**, 062135 (2013).
- [23] R. Zia, E. Praestgaard, and O. Mouritsen, *American Journal of Physics* **70**, 384 (2002).
- [24] E. Boksenbojm, C. Maes, K. Netočný, and J. Pešek, *EPL (Europhysics Letters)* **96**, 40001 (2011).
- [25] J. Bisquert, *American Journal of Physics* **73**, 735 (2005).
- [26] A. M. Walczak, A. Mugler, and C. H. Wiggins, *Proceedings of the National Academy of Sciences* **106**, 6529 (2009).
- [27] A. Savitzky and M. J. Golay, *Analytical Chemistry* **36**, 1627 (1964).
- [28] G. Altan-Bonnet and R. N. Germain, *PLoS Biology* **3**, e356 (2005).
- [29] N. Friedman, L. Cai, and X. S. Xie, *Physical Review Letters* **97**, 168302 (2006).
- [30] A. Mugler, A. M. Walczak, and C. H. Wiggins, *Physical Review E* **80**, 041921 (2009).
- [31] J. W. Cotari, G. Voisinne, O. E. Dar, V. Karabacak, and G. Altan-Bonnet, *Science Signaling* **6**, ra17 (2013).

Supplementary information

CRITICAL VS. BIOCHEMICAL PARAMETERS

The criticality parameters n_c , θ , and h are given by Eq. 6 in the main text. For convenience, Table I gives the values of n_c and the expansion coefficients f_{n_c} , f'_{n_c} , and f'''_{n_c} , on which θ and h depend, in terms of the biochemical parameters of the Schlögl and Hill models. Table I also gives the algebraic inverse: expressions for the biochemical parameters a , s , and K in terms of the criticality parameters. In the Hill model H is an additional free parameter.

EXPERIMENTAL METHODS

The experimental data, along with a detailed description of the experimental methods, have been published previously in Ref. [13] of the main text. For the sake of completeness, in this section we briefly summarize the experimental

	Schlögl	Hill
Feedback function	$f_n = \frac{aK^2 + s(n-1)(n-2)}{(n-1)(n-2) + K^2}$	$f_n = a + s \frac{n^H}{n^H + K^H}$
Critical value (at which $f''_{n_c} = 0$)	$n_c = \frac{3}{2} + \frac{1}{6} \sqrt{3(4K^2 - 1)}$	$n_c = K \left(\frac{H-1}{H+1} \right)^{1/H}$
Expansion coefficients	$f_{n_c} = \frac{(3a+s)K^2 - s}{4K^2 - 1}$ $f'_{n_c} = (s - a)K^2 \left(\frac{3}{4K^2 - 1} \right)^{3/2}$ $f'''_{n_c} = -6(s - a)K^2 \left(\frac{3}{4K^2 - 1} \right)^{5/2}$	$f_{n_c} = a + \left(\frac{H-1}{2H} \right) s$ $f'_{n_c} = \frac{(H^2 - 1)s}{4Hn_c}$ $f'''_{n_c} = -\frac{(H^2 - 1)^2 s}{8Hn_c^3}$
Inversion (where $x \equiv 2n_c - 3$)	$K^2 = \frac{1}{4}(3x^2 + 1)$ $s = \frac{3n_c^3(\theta+h) + n_c x^2 + x^3}{3n_c^2 \theta + x^2}$ $a = \frac{(3x^2 + 1)[3n_c^3(\theta+h) + n_c x^2 + x^3] - 4x^5}{(3x^2 + 1)(3n_c^2 \theta + x^2)}$	$K = n_c \left(\frac{H+1}{H-1} \right)^{1/H}$ $s = n_c \frac{16H}{(H^2 - 1)[(H^2 - 1)\theta + 4]}$ $a = n_c \frac{(H-1)[(H+1)^2(\theta+h) + 4]}{(H+1)[(H^2 - 1)\theta + 4]}$

TABLE I: Expressions relating criticality parameters n_c , θ , and h to biochemical parameters a , s , and K (and H in the Hill model).

system and methods.

The data investigate the inhibition of a complex signaling cascade, the antigen-driven MAP kinase activation in primary CD8+ mouse T cells. A natural way to stimulate T cells is to load a peptide, that is, a fragment of an antigenic protein (which the T cells are programmed to recognize), onto antigen-presenting cells. We achieve this by incubating RMA-S cells with antigen at 37 °C. At the same time, we harvest the spleen and lymph nodes of a RAG2^{-/-} OT1 mouse which has T cells specific only to the ovalbumin peptide with the amino acid sequence SIINFEKL. When we mix the OT1 T cells with the antigen-loaded RMA-S cells, we expose the OT1 T cells to their activating peptide. In response, the T cells activate their receptors through a SRC Family kinase (Lck). This triggers an enzymatic cascade through Ras-Raf-MEK-ERK leading to double phosphorylation of ERK, rendering it capable of communicating with the nucleus. The distribution of the abundance of doubly phosphorylated ERK (ppERK), a key factor in cell regulation, is the readout in Fig. 3 of the main text.

To measure the abundance of ppERK, we use fluorescence cytometry. Specifically, we introduce ppERK-targeted antibodies that are pre-conjugated with a fluorescent dye. Because antibodies are very effective at selectively attaching to their target molecule with negligible false-positives, the fluorescence intensity of the dye is proportional to the abundance of ppERK. To measure the intensity, approximately 30,000 cells per sample are passed one-by-one through a microfluidic device where they encounter a series of excitation lasers. Each cell yields one intensity value, and the histogram provides an estimate of the distribution of ppERK abundance across the population. We assume that the distribution across the population is a fair representation of the steady-state distribution of ppERK abundance of a single cell. This is reasonable (and is the accepted practice) since while the cells are alive and the experiment is taking place, they are in a dilute suspension (approximately 30,000 cells in 100 μ L), not close enough together to influence each other.

Cells are treated with various doses of inhibitory drugs. The drugs and dose ranges used in the experiments are given in Table II. In Figs. 3(c) of the main text, 6, and 7, the size of the data point is proportional to the log of the dose (with the smallest size being 0 nM), and the shape of the data point indicates the drug, as listed in Table II.

Ref. [13] describes a biologically-driven analysis of the data by fitting to a Gaussian mixture model, together with

Drug	Inhibits	Dose range (nM)	Shape of data point
PD325901	MEK	0.09–1000	Up-pointing triangle
AZD6244	MEK	2.4–5000	Down-pointing triangle
Trametinib	MEK	0.5–1000	Right-pointing triangle
Dasatinib	SRC	0.09–1000	Circle
Bosutinib	SRC	0.5–1000	Square
PP2	SRC	24–50,000	Diamond

TABLE II: Drugs and dose ranges used in the experiments. Doses are spaced logarithmically. Shapes are used for the data points in Figs. 3(c), 6, and 7.

more experiments which correlate the inhibition to a functional read-out days after the stimulus. Ref. [13] also proposes a biologically-motivated coarse-grained model that relies on detailed knowledge of the MAP-kinase cascade. Here we employ an orthogonal approach: we focus on understanding the universal features, making as few assumptions as possible, and requiring no prior knowledge of the biology.

EXPERIMENTAL DATA ANALYSIS

Due to the long-tailed nature of the experimental molecule number distributions, it is more numerically stable to analyze them in log space. Here we provide the necessary conversions between functions of the molecule number from our theory, and functions of the log intensity from the experiments. In this section, prime denotes a derivative of a function with respect to its argument (n for f ; ℓ for q , Q , and ϕ).

Variables

The intensity is proportional to molecule number, $I = I_1 n$, where I_1 is the intensity of one molecule. We record and analyze the log intensity $\ell = \log I$. Therefore we have

$$\ell = \log(I_1 n), \quad n = \frac{e^\ell}{I_1}. \quad (9)$$

Probability distributions

The molecule number distribution is p_n . Denote the distribution of ℓ as $q(\ell)$. Approximating n as continuous, probability conservation requires $p_n dn = q(\ell) d\ell$. Therefore

$$q(\ell) = \frac{p_n}{d\ell/dn} = np_n. \quad (10)$$

Feedback function

The feedback function is related to the probability distribution according to $f_n = np_n/p_{n-1}$ as in the main text. Using Eq. 10, the feedback function is written

$$f_n = \frac{np_n}{p_{n-1}} = (n-1) \frac{np_n}{(n-1)p_{n-1}} = (n-1) \frac{q(\ell)}{q(\tilde{\ell})}, \quad (11)$$

where, using Eq. 9,

$$\tilde{\ell} = \log[I_1(n-1)] = \log(I_1 n) + \log(1 - \epsilon) \approx \ell - \epsilon. \quad (12)$$

The last steps define $\epsilon \equiv 1/n$ and assume that for most values of n with appreciable probability we have $\epsilon \ll 1$. Therefore Eq. 11 becomes

$$\begin{aligned} f_n &= n(1 - \epsilon) \frac{q(\ell)}{q(\ell - \epsilon)} \approx n(1 - \epsilon) \frac{q(\ell)}{q(\ell) - \epsilon q'(\ell)} = \frac{n(1 - \epsilon)}{1 - \epsilon q'/q} \approx n(1 - \epsilon) \left(1 + \epsilon \frac{q'}{q} \right) \approx n \left[1 + \epsilon \left(\frac{q'}{q} - 1 \right) \right] \\ &= n + \frac{q'}{q} - 1, \end{aligned} \quad (13)$$

where we have kept only to first order in ϵ . Defining $\phi(\ell) \equiv f_n - n$, from Eq. 13 we have

$$\phi(\ell) = f_n - n = \frac{q'}{q} - 1 = Q'. \quad (14)$$

In the last step we define

$$Q(\ell) \equiv -\ell + \log q \quad (15)$$

so that ϕ is computed as a total derivative, which we find more numerically stable.

Maxima

Maxima are defined by $p'_{n_*} = 0$. Eq. 9 implies

$$\partial_n = I_1 e^{-\ell} \partial_\ell \quad (16)$$

Therefore, using Eqs. 9 and 10, the maxima condition reads

$$0 = \partial_n p = (I_1 e^{-\ell} \partial_\ell) \left(\frac{q}{n} \right) = I_1 e^{-\ell} \partial_\ell (I_1 e^{-\ell} q) = I_1^2 e^{-\ell} (-e^{-\ell} q + e^{-\ell} q') = (I_1 e^{-\ell})^2 (q' - q). \quad (17)$$

We define points ℓ_* by

$$q'(\ell_*) = q(\ell_*). \quad (18)$$

Equivalently, by Eq. 14, the ℓ_* satisfy

$$\phi(\ell_*) = 0, \quad (19)$$

which is consistent with the interpretation of ϕ as the forcing. The maxima are obtained via Eq. 9:

$$n_* = \frac{e^{\ell_*}}{I_1}. \quad (20)$$

Critical point

The critical point n_c is defined by $f''_{n_c} = 0$. Using Eq. 16, this condition reads

$$0 = \partial_n^2 f = \partial_n^2 (\phi + n) = \partial_n^2 \phi = (I_1 e^{-\ell} \partial_\ell)^2 \phi = I_1 e^{-\ell} \partial_\ell (I_1 e^{-\ell} \partial_\ell \phi) = I_1^2 e^{-\ell} (-e^{-\ell} \phi' + e^{-\ell} \phi'') = (I_1^2 e^{-\ell})^2 (\phi'' - \phi'). \quad (21)$$

We define a point ℓ_c by

$$\phi''(\ell_c) = \phi'(\ell_c), \quad (22)$$

and the critical point n_c is obtained via Eq. 9:

$$n_c = \frac{e^{\ell_c}}{I_1}. \quad (23)$$

Numerically we enforce Eq. 22 by writing it as $0 = \partial_\ell (\phi' - \phi)$, and therefore

$$\ell_c = \operatorname{argmax}_\ell (\phi' - \phi). \quad (24)$$

Derivatives

Derivatives of f with respect to n at n_c are related in a straightforward way to derivatives of ϕ with respect to ℓ at ℓ_c . First, the zeroth derivative is, by Eq. 14,

$$f_{n_c} = \phi(\ell_c) + n_c, \quad (25)$$

where n_c is given by Eq. 23. Then, using Eq. 16, the first derivative is

$$f'_{n_c} = \partial_n[\phi + n]_{n_c} = \partial_n[\phi]_{n_c} + 1 = [(I_1 e^{-\ell} \partial_\ell \phi)]_{\ell_c} + 1 = I_1 e^{-\ell_c} \phi'(\ell_c) + 1 = \frac{\phi'(\ell_c)}{n_c} + 1. \quad (26)$$

Finally, by a similar procedure, the third derivative is

$$f'''_{n_c} = \frac{1}{n_c^3} [\phi'''(\ell_c) - 3\phi''(\ell_c) + 2\phi'(\ell_c)] = \frac{1}{n_c^3} [\phi'''(\ell_c) - \phi'(\ell_c)], \quad (27)$$

where the second step uses Eq. 22.

Criticality parameters

Using Eqs. 23, 25-27, and 20, the criticality parameters defined in Eq. 6 of the main text are

$$m = \frac{n_* - n_c}{n_c} = e^{\ell_* - \ell_c} - 1, \quad (28)$$

$$\theta = \frac{2(1 - f'_{n_c})}{-f'''_{n_c} n_c^2} = \frac{-2\phi'(\ell_c)}{\phi'(\ell_c) - \phi'''(\ell_c)}, \quad (29)$$

$$h = \frac{2(f_{n_c} - n_c)}{-f'''_{n_c} n_c^3} = \frac{2\phi(\ell_c)}{\phi'(\ell_c) - \phi'''(\ell_c)}. \quad (30)$$

Note that they do not depend on I_1 .

Savitsky–Golay filtering

To estimate derivatives, we apply Savitsky–Golay filtering to $q(\ell)$. Savitsky–Golay filtering replaces each data point with the value of a polynomial of order J that is fit to the data within a window W of the point. Since we require three derivatives of $\phi(\ell)$ (Eqs. 29 and 30), which depends on the first derivative of $q(\ell)$ (Eq. 14), we use the minimum value $J = 4$.

Analysis procedure

The analysis is demonstrated for an example experimental condition in Fig. 4. In summary, we:

1. plot $q(\ell)$ from the data using L bins [Fig. 4(a), black];
2. filter $q(\ell)$ using window W [Fig. 4(a), red];
3. compute ℓ_* using Eq. 19 [Fig. 4(b)];
4. compute ℓ_c using Eq. 24 [Fig. 4(c)];
5. compute m , θ , and h from ℓ_c , ℓ_* , and ϕ and its derivatives using Eqs. 28-30;
6. compute p_n from the data using I_1 ; and
7. compute C/k_B from p_n , θ , n_c (Eq. 23), f'''_{n_c} (Eq. 27), and f_n (Eq. 13) using Eq. 8 of the main text.

Fig. 4(d) shows the values of ℓ_* and ℓ_c overtop the intensity distribution $p(I)$. We see that the maxima fall where expected, and the critical point falls between the maxima as expected.

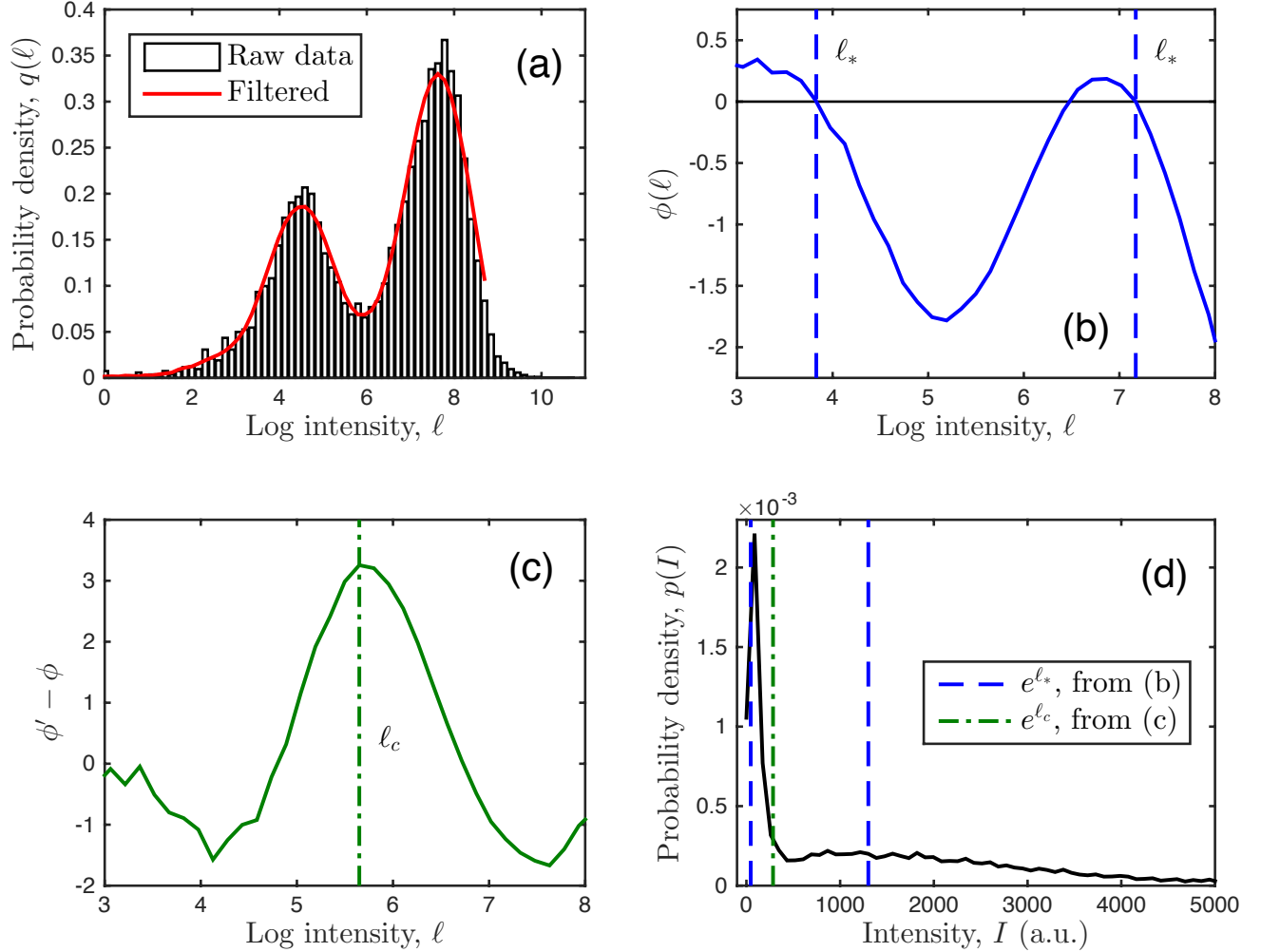


FIG. 4: Demonstration of analysis procedure for 3.4 nM of MEK inhibitor PD325901. (a) The distribution $q(\ell)$ of log intensity ℓ is plotted using $L = 100$ bins and Savitsky–Golay filtered using a window of $W = 25$ data points. (b, c) From the filtered data, we compute $\phi(\ell)$ to find ℓ_* , and $\phi' - \phi$ to find ℓ_c , as described in the text. (d) ℓ_* and ℓ_c give the maxima and critical point of the intensity distribution.

VALIDATION OF ANALYSIS

We validate the analysis in several ways, as described in the main text. One way is to investigate the effects of MEK and SRC inhibition on the high-molecule-number state. As described in Ref. [13] of the main text, previous work demonstrated that MEK inhibition drives the high state to lower molecule numbers, whereas SRC inhibition does not. Fig. 5 shows the results of our analysis for MEK inhibitor PD325901 [Fig. 5(a)] and SRC inhibitor Dasatinib [Fig. 5(b)]. We see that MEK inhibition drives the high-intensity stable fixed point to lower molecule numbers, whereas SRC inhibition does not, in agreement with the previous work.

ROBUSTNESS OF RESULTS

Typically when working with distributions, the number of bins is an adjustable parameter. However, since here we also filter the distribution, changing the filter window is similar to changing the number of bins. That is, choosing a large number of bins L , but also a large window size $W < L$, is similar to choosing a small L . Therefore, we choose L to be sufficiently large to resolve the main features of the distribution, then focus on the adjustable parameter W/L .

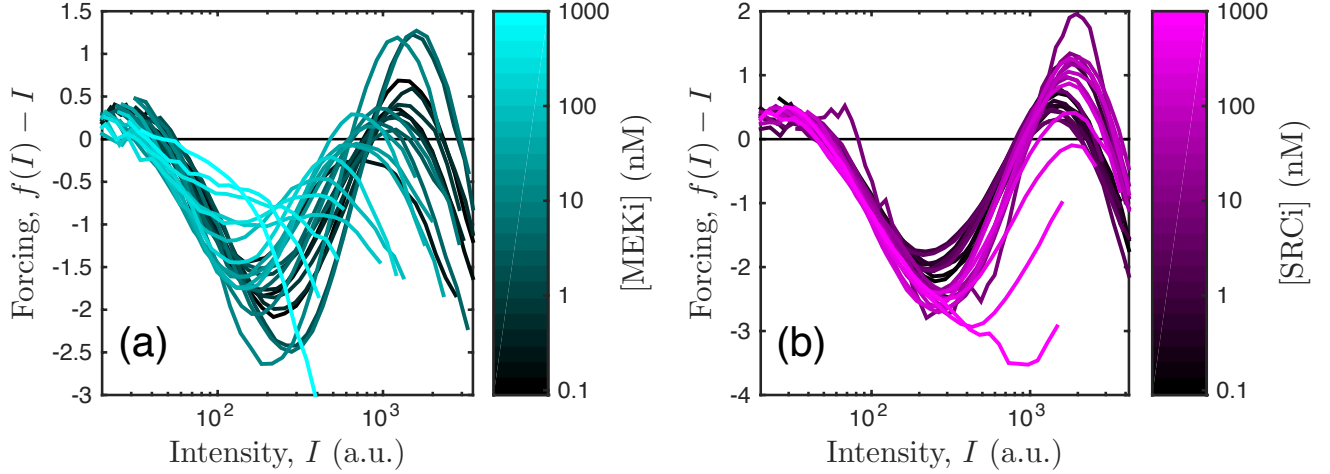


FIG. 5: Forcing function [equivalent to $\phi(\ell)$] at various doses of (a) MEK inhibitor PD325901 and (b) SRC inhibitor Dasatinib. We see that MEK inhibition drives the high-intensity stable fixed point to lower molecule numbers, whereas SRC inhibition does not, as expected from previous work.

We find that $L = 100$ suffices (although we check L as low as 50 in what follows).

In principle, the parameter W/L varies from 0 to 1. $W/L = 0$ corresponds to no filtering, whereas $W/L = 1$ corresponds to using every data point in the filter, i.e., extreme over-filtering. In the main text we use $W/L = 25/100 = 0.25$ (Fig. 3). Here we investigate the robustness of the results to the value of W/L , focusing in particular on the behavior of the order parameter in Fig. 3(c) of the main text. As shown in Fig. 6, we vary W/L over the range 0.15 to 0.5 in two ways: we either vary W [Fig. 6(a)-(b)] or we vary L [Fig. 6(c)-(d)]. We see in Fig. 6 that in both cases, the theory and the experimental data continue to agree in the same important ways noted in the main text: (i) no data exist between the branches; (ii) data near $m = \theta = 0$ have $h \approx 0$ (yellow); (iii) the data closely follow the lower branch and obey $m \geq -1$; and (iv) the data exhibit the steep rise of the upper branches in the biochemical models.

AUTOFLUORESCENCE

All cells, without any attached fluorescent antibodies, emit a wide range of frequencies at low intensity in response to the exciting lasers, called autofluorescence. The presence of autofluorescence means that the low-intensity readings in most flow cytometry experiments include contributions due inherently to the measurement technique. Here, it is possible that this effect increases the size of the low-intensity peak beyond the actual fluorescence intensity of ppERK. A larger low-intensity peak and a long tail are features that are consistent with negative values of the external field h , since negative h corresponds to biasing the peak of the distribution toward lower molecule numbers. Thus, autofluorescence may contribute to the fact that the data exhibit $h \lesssim 0$, as seen in Fig. 3(c) of the main text.

ABSOLUTE MOLECULE NUMBER

Absolute molecule number is set by the parameter I_1 . The heat capacity C provides a way to calibrate I_1 . Fig. 7 shows C for the theory and the experimental data using four values of I_1 over four orders of magnitude. In all cases, we see that both the theory and the data exhibit a global minimum at $\theta = h = 0$, which is a key prediction of the universality class ($\alpha = 0$). However, for $I_1 = 10$ [Fig. 7(a)] and $I_1 = 1$ [Fig. 7(b)] the minimum of the theory is higher than that of the data, while for $I_1 = 0.01$ [Fig. 7(d)] the minimum of the theory is lower than that of the data. Only for $I_1 = 0.1$ [Fig. 7(c); also Fig. 3(c) inset of main text] are the minima the same depth. We conclude that $I_1 = 0.1$ is the correct value, which corresponds, for example, to a value of $\bar{n}_c = 7,300$ molecules averaged across all experiments, and a value of $\bar{n}_* = 35,000$ molecules in the high mode averaged across all cases with no inhibitor.

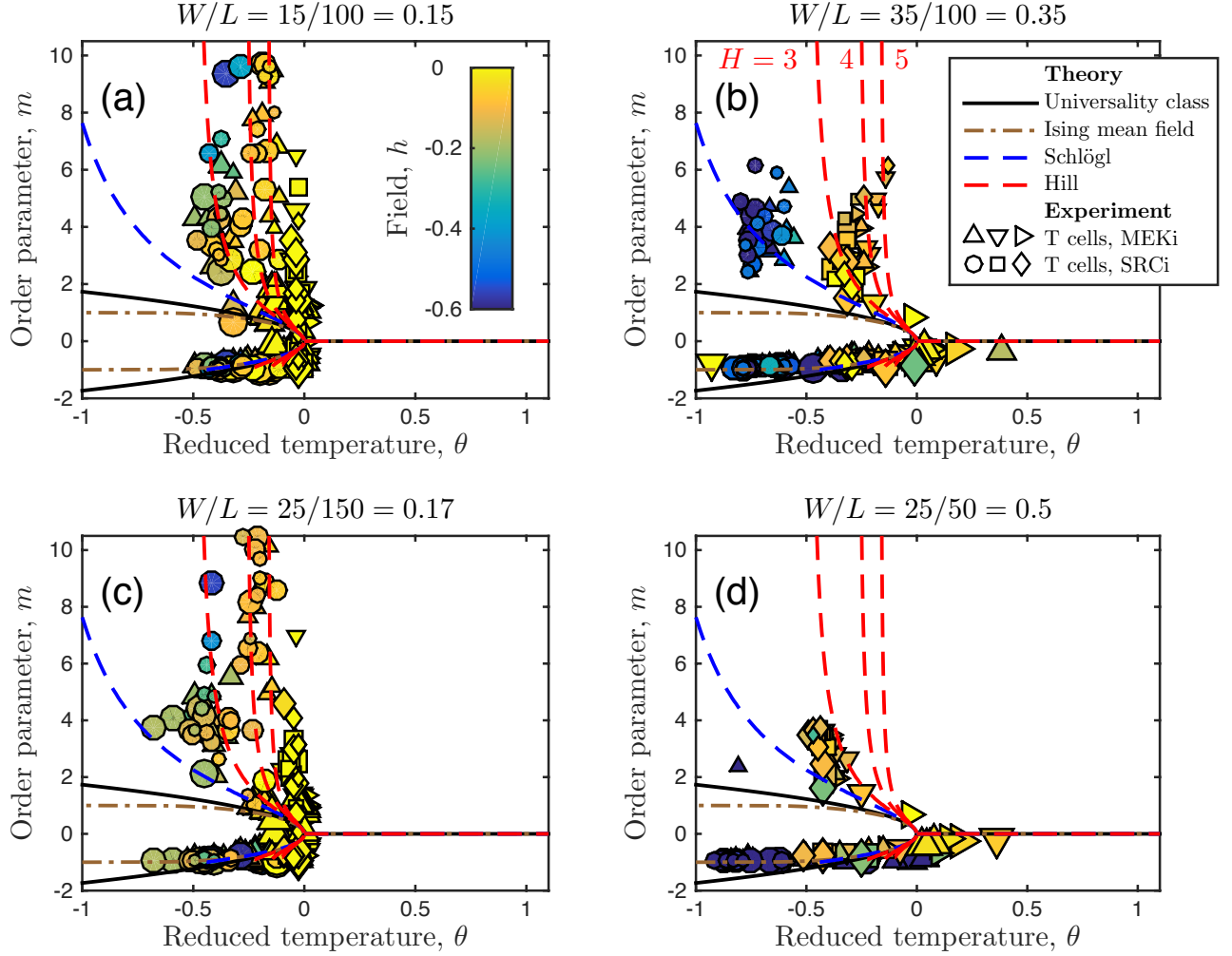


FIG. 6: Main features are robust to choice of W/L , as described in the text. Title of each panel indicates choices of W and L . See Table II for drugs (shape) and doses (size). Colorbar, legend, and H values in (a) and (b) apply to all panels. All theory curves take $h = 0$.

The value of 35,000 ppERK molecules is consistent with previous measurement on these cells described in Ref. [28] of the main text. In that reference it was estimated that there are approximately 100,000 ERK molecules per cell, but only about 30% of these, or about 30,000 molecules, are doubly phosphorylated during T cell receptor activation. Thus, the heat capacity allows us to calibrate I_1 unambiguously and allows estimation of absolute molecule number from fluorescence data with strikingly plausible results.

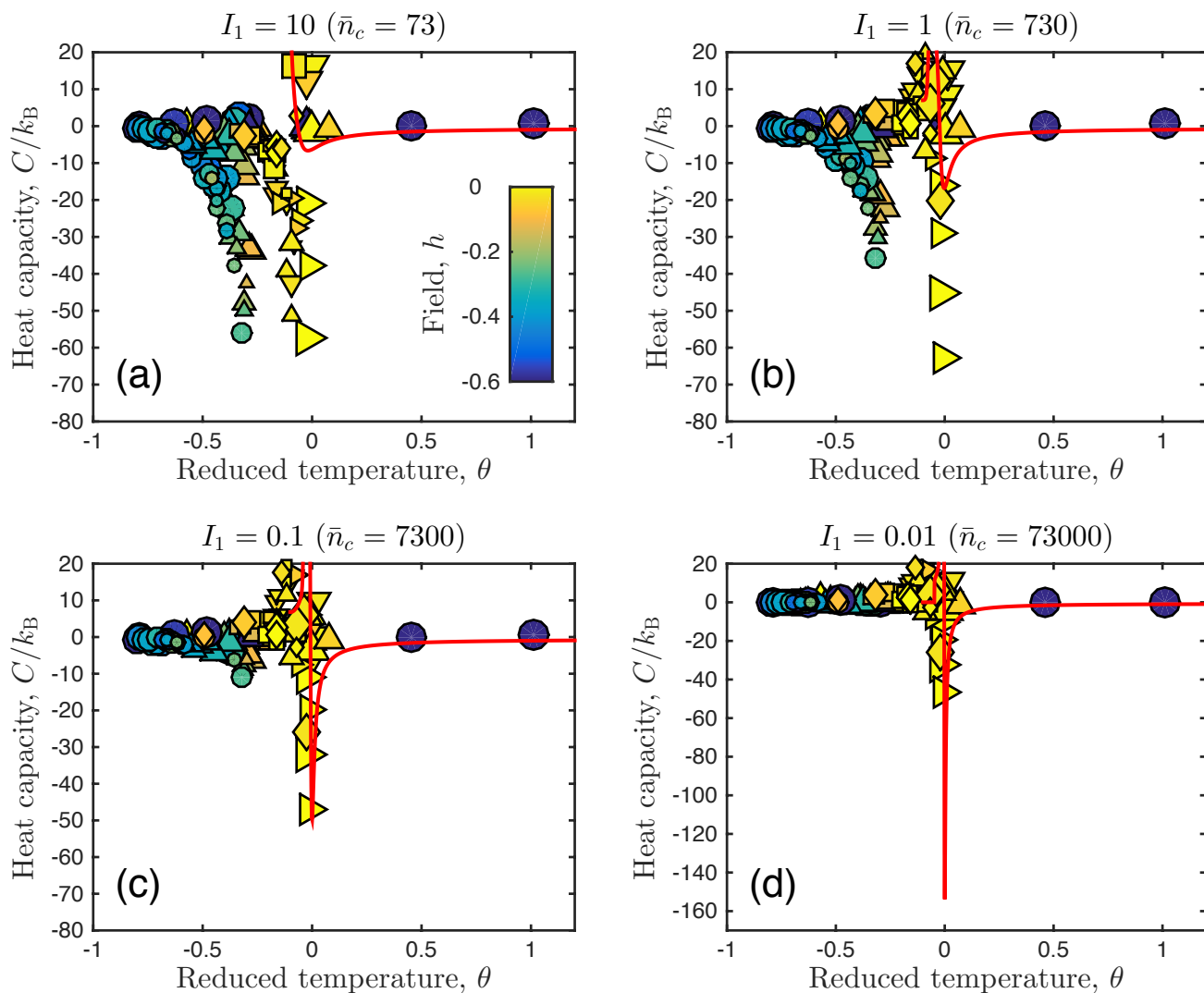


FIG. 7: Comparison of heat capacity theory with experimental data allows determination of I_1 , and therefore absolute molecule number. Titles of each panel indicate values of I_1 , and the corresponding value of \bar{n}_c averaged across all experiments. Only in (c) are the depths of the global minima in the theory and data the same. See Table II for drugs (shape) and doses (size). Colorbar in (a) applies to all panels. Theory curves are for Hill model with $h = 0$ and $H = 4$.